Green Chemistry

PAPER

View Article Online
View Journal | View Issue

Cite this: *Green Chem.*, 2025, **27**, 2538

Green extraction of polyphenolic lignin using $FeCl_3$-mediated tartaric acid-DES and its derived lignin nanoparticles for enhancing the application performance of PVA film in green agriculture†

Yadan Luo,[a] Linlin Liang,[a,b] Huaying Luo,[c] Fanyan Zeng,[a] Chengrong Qin,*[a] Chen Liang,[a] Baojie Liu,[a] Caoxing Huang[b] and Shuangquan Yao*[a]

Lignin nanoparticles (LNPs) address the challenges associated with the complex chemical structure and high molecular weight of lignin, thereby facilitating green value-added transformations. However, the heterogeneity of lignin significantly influences the self-assembly behavior of LNPs. To obtain lignin with optimal performance for the preparation of LNPs, a novel deep eutectic solvent (DES) featuring a robust hydrogen bond network (choline chloride/tartaric acid-$FeCl_3$, CC/TA-$FeCl_3$) was developed in this study. Extracted lignin exhibited a higher phenolic hydroxyl content and lower molecular weight. Specifically, the phenolic hydroxyl content (2.90 mmol g^{-1}) increased by 15.54% compared to that extracted using (CC/lactic acid-$FeCl_3$ (CC/LA-$FeCl_3$)). Amphiphilic nanoparticles were synthesized *via* layer-by-layer self-assembly utilizing van der Waals forces and π–π interactions. They had a narrow particle size distribution (21–76 nm) and a small average particle size (35.33 nm). They exhibited a highly negative zeta potential of −31.25 mV and demonstrated effective free radical scavenging efficiency (79.87%). The water dispersion stability over 72 h was improved by 200%. The LNPs significantly enhanced the UV resistance (80%), tensile strength (72%), and hydrophobic characteristics (125%) of PVA films. LNPs/PVA film provides the feasibility for the high-quality development of green agriculture. These results provide a new approach for the green transformation of lignin through the preparation of efficient extraction and preparation of high-performance LNPs.

Received 18th December 2024,
Accepted 5th February 2025

DOI: 10.1039/d4gc06405d

rsc.li/greenchem

Green foundation

1. We report a green, efficient and sustainable pretreatment strategy for deep eutectic solvent (DES). Based on the acid multisite coordination theory of tartaric acid, $FeCl_3$-mediated tartaric acid-DES was formed by competition with the monodentate iron ligand. With this strategy, we can achieve high efficiency and high purity extraction of lignin from biomass under mild green chemical conditions.
2. The lignin extracted has low molecular weight and high phenolic content. The heterogeneity and poor dispersion of lignin in high value conversion were solved by preparing homogeneous lignin nanoparticles (LNPs). The LNPs/PVA composite films have good hydrophobic properties, UV resistance and tensile strength. We propose a "green" concept, starting from simple raw materials, through mild green reaction conditions.
3. In the future, new DES systems will be constructed using supported Lewis acids instead of traditional Lewis acids. It has higher selectivity for lignin ether bond cleavage, and is environmentally friendly, with good recovery and recycling, which will help promote the development of green chemistry.

Introduction

Lignin is a natural polyphenol characterized by its biodegradability and cost-effectiveness.[1] There is growing interest among researchers in utilizing lignin as a green material that offers both economic and environmental advantages. However, the green high-value utilization of lignin is constrained by poor dispersion, heterogeneity, and limited availability of active

[a]*Guangxi Key Laboratory of Clean Pulp & Papermaking and Pollution Control, School of Light Industrial and Food Engineering, Guangxi University, Nanning, 530004, PR China. E-mail: yaoshuangquan@gxu.edu.cn, qinchengrong@gxu.edu.cn*
[b]*Jiangsu Co-Innovation Center of Efficient Processing and Utilization of Forest Resources, Nanjing Forestry University, Nanjing, 210037, PR China*
[c]*Xianhe Co., Ltd, Quzhou, 324022, PR China*
† Electronic supplementary information (ESI) available. See DOI: https://doi.org/10.1039/d4gc06405d

sites.[2] Consequently, lignin is underutilized compared with cellulose. Compared to bulk lignin, lignin nanoparticles (LNPs) exhibit superior physical and chemical properties. They exhibit homogeneous dispersion and possess an abundance of surface functional groups. Consequently, the conversion of lignin into LNPs represents a significant strategy for addressing inherent challenges and exploiting the high value of lignin.[3] LNPs are formed through self-assembly facilitated by van der Waals forces and π–π stacking, leading to the formation of hydrophilic aggregates. Their formation is attributed to the synergistic effect of the hydrophilic (hydroxyl and carboxyl) and hydrophobic (phenyl) groups of lignin.[4] In particular, the modulation of phenolic hydroxyl in lignin is crucial for the preparation of LNPs. Previous studies have demonstrated that lignin rich in phenolic hydroxyl groups can be extracted using a deep eutectic solvent (DES) during the biomass component green separation.[5–7] This suggests that green efficient separation of lignin rich in phenolic hydroxyl using DES can lead to the preparation of LNPs with superior properties.

The interaction between the hydrogen bond donor (HBD) and hydrogen bond acceptor (HBA) in DES provides dual acid–base catalysis and establishes a strong hydrogen bond network. The controlled cleavage of the ether bonds between the lignin phenylpropane units is facilitated. Lignin from lignocellulosic biomass was extracted using a conventional binary DES.[8,9] However, achieving highly efficient lignin phenolization remains a challenge.[10] These results indicate that Lewis acids enhance the phenolization efficiency of lignin in DES. As electrophilic reagents, Lewis acids can participate in electrophilic substitution reactions at the *ortho* and *para* positions relative to the methoxy or phenolic hydroxyl in lignin. The removal of the methoxy group and the formation of a newly generated phenolic hydroxyl enhance the reactivity of lignin.[11] Shen *et al.*[12] incorporated $FeCl_3$ into a choline chloride/lactate DES and observed a lignin separation yield of 62.1%, while the phenolic hydroxyl content of lignin reached 3.8 mmol g^{-1}. Owing to its two carboxyl groups and two hydroxyl groups, tartaric acid serves as an effective hydrogen bond donor.[13] A DES with a strong hydrogen bonding network is constructed by coordinating tartaric acid (TA) with a hydrogen bond acceptor (choline chloride, CC). This indicates that more green efficient separation and phenolization of lignin can be achieved using $FeCl_3$-mediated CC/TA DES. The bottleneck in the high-value conversion of lignin was overcome by preparing LNPs with excellent performance.

To simultaneously increase lignin separation and phenolization efficiency, we designed a ternary DES using tartaric acid as a hydrogen bond donor to develop a highly applicable strategy for obtaining small-molecule polyphenolic hydroxyl lignin (Fig. 1). The strong hydrogen bond network of this system promotes the breaking of the aromatic ether bonds of lignin, and the resulting phenyl units are phenolized by $FeCl_3$ to form polyphenolic hydroxyl lignin. The LNPs prepared from this lignin exhibit excellent characteristics of uniform dispersion

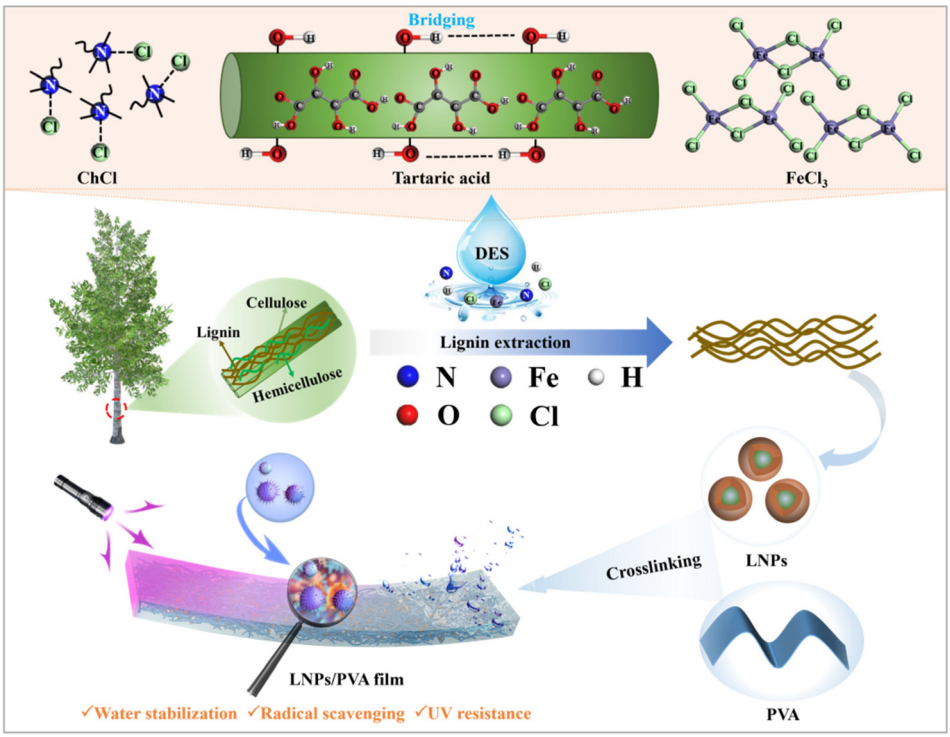

Fig. 1 Separation of polyphenolic lignin based on the design principle of tartaric acid-DES and its derived lignin nanoparticles for enhancing the performance of PVA films.

and prolonged stability. Finally, the LNPs and PVA were mixed to prepare a composite film, and the performance of the LNPs was evaluated. The LNPs significantly improved the hydrophobicity, UV resistance, free radical scavenging ability, and mechanical properties of the composite film. The novelty of this work lies in the synthesis of a functional DES capable of simultaneous lignin separation and phenolization and its application in the component separation of lignocellulosic biomass. Therefore, this study provides a green strategy for the acquisition of polyphenolic hydroxyl lignin and the high-quality application of PVA film in green agriculture.

Results and discussion

Construction and characterization of CC/TA-$FeCl_3$ novel DES

The bimolecular conformation and bond length information of the system containing 2 mol CC and 1 mol TA were analyzed[14] (Fig. 2). Fig. 2a shows the molecular conformations and bond lengths of various bimolecular systems. Fig. 2b illustrates the hydrogen-bonding sites and energies of these systems. The hydroxyl group (–OH) on lactic acid (LA) forms a chlorine–hydrogen (Cl–H) hydrogen bond with a chlorine atom on CC. The hydroxyl group (–OH) on TA, in addition to

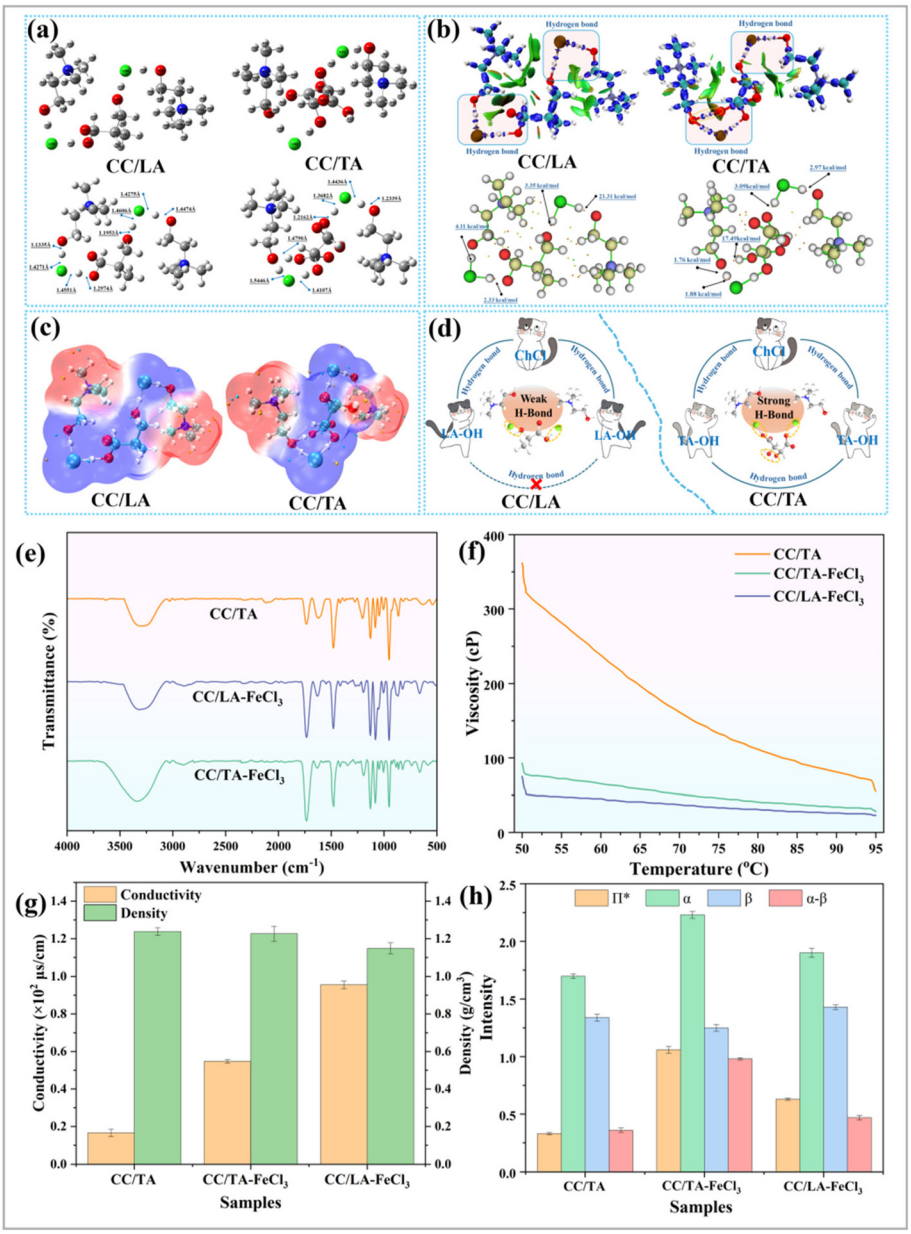

Fig. 2 Structural characteristics and chemical properties of different DES systems. (a) Bimolecular conformation and bond length information; (b) bimolecular hydrogen bond position and bond energy; (c) electrostatic potential of bimolecular system; (d) DES hydrogen bond connection diagram; (e) bimolecular infrared spectroscopy; (f) bimolecular viscosity analysis; (g) conductivity and density; (h) solvent solvatochromic parameters.

forming Cl–H bonds with CC, can participate in intramolecular hydrogen bonding because of the presence of multiple hydroxyl groups on TA. Consequently, CC/TA can form stronger hydrogen-bond networks. Fig. 2c shows the electrostatic interactions between CC and TA or LA (Fig. 2c). LA and TA molecules show a distinct blue distribution because the oxygen atom in the hydroxyl group has high electron affinity, making the molecule electronegative. In particular, the blue regions of the TA molecules were more extensive and pronounced, which was attributed to the higher number of hydroxyl groups present in TA. CC shows a pink distribution, indicating a positive charge. The range of positive and negative potentials suggests that CC, LA, and TA are predisposed to electrostatic interactions, resulting in a more stable bimolecular system. This indicates that the DES formed by the combination of TA and CC can establish a more robust hydrogen bond network (Fig. 2d).

Fig. 2(e–h) shows the chemical properties of the three DES systems: CC/TA, CC/TA-$FeCl_3$, and CC/LA-$FeCl_3$. FT-IR revealed significant stretching vibration peaks of the hydroxyl group (–OH) in the range of 3600–3000 cm^{-1} across all three systems (Fig. 2e). This suggests the presence of intermolecular hydrogen bond networks in all three DES systems.[15] Fig. 2f illustrates the changes in the viscosity of the three DES systems with increasing temperature. At an initial temperature of 50 °C, the viscosities of CC/TA, CC/TA-$FeCl_3$, and CC/LA-$FeCl_3$ were measured to be 362, 93, and 77 cP, respectively. The incorporation of $FeCl_3$ not only introduced additional acidic sites but also markedly decreased the viscosity of CC/TA. The CC/TA-$FeCl_3$ system exhibits enhanced penetration efficiency.[16] Interestingly, the viscosity of CC/TA-$FeCl_3$ decreases significantly with increasing temperature. The viscosity was 28 cP at 95 °C (CC/LA-$FeCl_3$ viscosity of 22 cP). This shows that viscosity does not affect the separation efficiency of CC/TA-$FeCl_3$ for lignin at higher temperatures.

Fig. 2g shows the densities and conductivities of the three DES systems. The densities of CC/TA, CC/TA-$FeCl_3$, and CC/LA-$FeCl_3$ are 1.24, 1.23, and 1.15 g cm^{-3}, respectively. No significant differences were observed between the groups. The electrical conductivities were measured to be 16.59, 54.8, and 95.6 μS cm^{-1} for the respective systems. The conductivity of CC/TA-$FeCl_3$ was lower than that of CC/LA-$FeCl_3$. This indicates that the number of free ions in this system was smaller, and the number of ions used to form hydrogen bonds was higher.[17] In addition, *K–T* parameters were used to quantify the chemical properties of the different DES systems. Fig. 2h presents the acidity (α) values, alkalinity (β) values, and polarizability (π*) of different DES. CC/TA-$FeCl_3$ exhibits the highest acidity (2.13). This suggests that the incorporation of $FeCl_3$ enhanced the acidity of the system. This facilitates the pyrolysis of lignin-carbohydrate complexes in the biomass, thereby enhancing the efficiency of lignin separation. The polarizabilities of CC/TA, CC/TA-$FeCl_3$, and CC/LA-$FeCl_3$ were 0.33, 1.06, and 0.63, respectively. The solubility of lignin is positively correlated with its polarizability. Consequently, CC/TA-$FeCl_3$ exhibits enhanced hydrogen bond donation and acceptance, as indicated by its acidity (α) value, alkalinity (β) value, and polarizability (π*).[18] This indicates that the novel DES system can establish a more stable hydrogen bonded network structure, thereby facilitating the separation of lignin.

Enhanced fractionation efficiency using CC/TA-$FeCl_3$

The effect of CC/TA-$FeCl_3$ treatment parameters on the separation efficiency of lignin was studied. Initially, the influence of varying the molar ratios of hydrogen bond acceptor (CC) and hydrogen bond donor (TA) on the separation efficiency during eucalyptus treatment was investigated (Fig. 3b). The hemicellulose separation yield increased with choline chloride incorporation, from 58.02% to 64.31%. Overall, this increase was not statistically significant. The lignin separation rate initially increased and then decreased with increasing choline chloride supplementation. The effective separation of lignin is challenging at elevated choline chloride levels. This phenomenon can be attributed to the fact that excessive CC increases the viscosity of the DES system, thereby reducing the permeability of the system. In addition, excessive HBA will lead to a decrease in the free and active groups that interact with lignin in the DES system, thereby reducing the separation efficiency of lignin.[19] This indicates that the separation efficiency of lignin depends on the synergistic effect between HBA and HBD. Therefore, the optimal choline chloride dosage was determined to be 2 mol.

Studies have demonstrated that DES provides more acidic sites with the addition of metal chlorides. A Lewis acid effect was observed during the treatment process. Additionally, the separation efficiency of hemicellulose and lignin was enhanced, thereby minimizing the energy consumption associated with the reaction.[20] The influence of the $FeCl_3$ concentration on the separation efficiency of the eucalyptus components was investigated within the CC/TA-$FeCl_3$ system (Fig. 3c). The separation yields of hemicellulose and lignin exhibited significant variation with increasing concentrations of $FeCl_3$; they both showed a trend of initially increasing and then decreasing. The turning point was observed at 0.11 M. An optimal concentration of $FeCl_3$ promoted the effective separation of hemicellulose and lignin. This phenomenon can be attributed to the synergistic effect of catalysis and acid hydrolysis, which facilitates their dissolution. At the same time, excess metal chloride increases the viscosity of the DES system, resulting in the inhibition of lignin separation. The lignin separation rate increased by 23.05% when the $FeCl_3$ concentration was 0.11 M, compared to its value at a concentration of 0.03 M. This indicates that an increase in the concentration of Lewis acids can significantly enhance the treatment efficiency. The incorporation of metal chlorides enhances the quantity of acidic sites and the ability to accept hydrogen bonds within the treatment system. Furthermore, Cl^- ions in the metal chlorides form hydrogen bonds with hydroxyl groups in lignin, thereby facilitating its dissolution.[21] Additionally, the cellulose separation efficiency exhibited minimal variation with increasing $FeCl_3$ concentration, stabi-

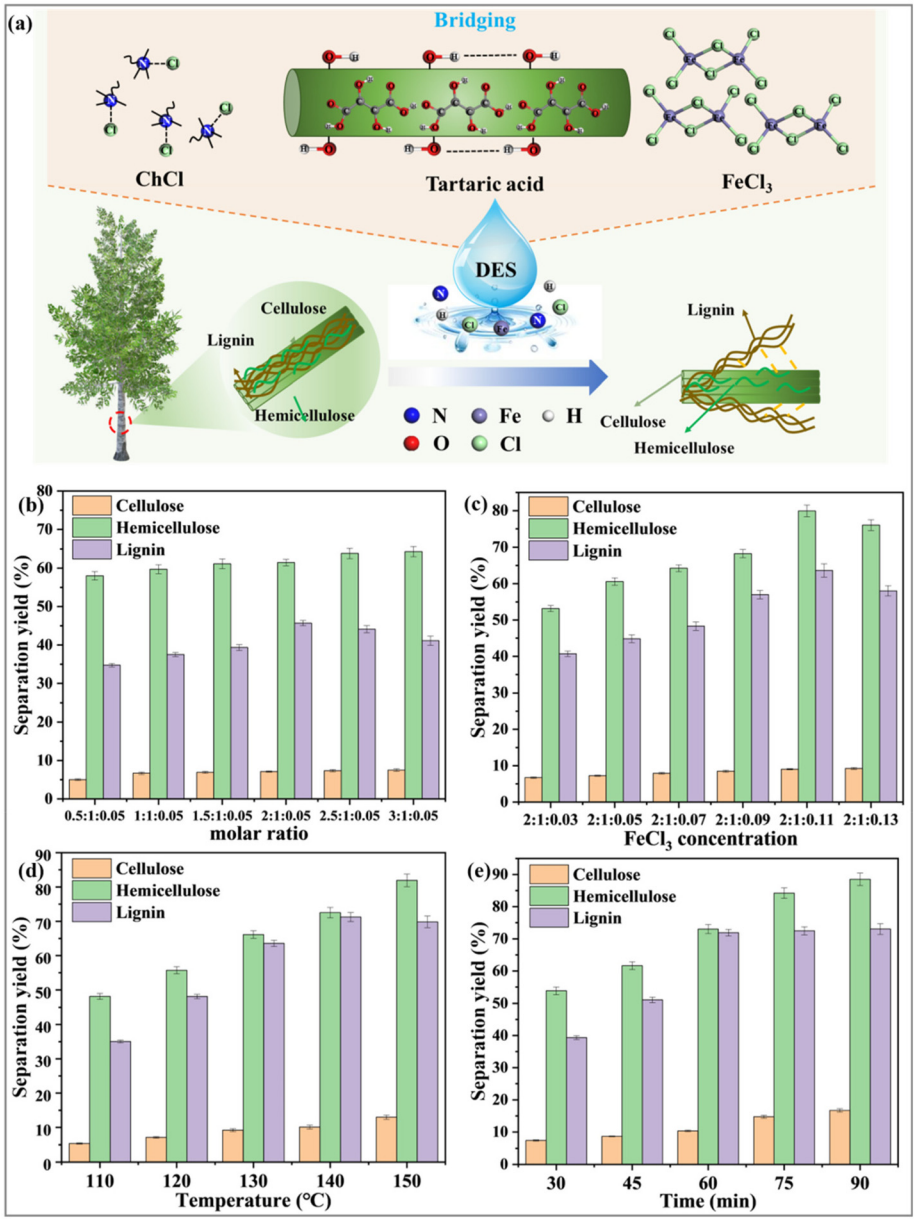

Fig. 3 Effects of different reaction conditions on the separation efficiency of eucalyptus wood components. (a) Schematic of lignin separation. (b) Molar ratio of CC/TA ($FeCl_3$ concentration: 0.05 M, reaction temperature: 130 °C, reaction time: 60 min). (c) Concentration of $FeCl_3$ (CC : TA = 2 M : 1 M, reaction temperature: 130 °C, reaction time: 60 min). (d) Reaction temperature (CC : TA : $FeCl_3$ = 2 M : 1 M : 0.11 M, reaction time: 60 min). (e) Reaction time (CC : TA : $FeCl_3$ = 2 M : 1 M : 0.11 M, reaction temperature: 140 °C).

lizing at approximately 8%. Therefore, 0.11 M is the optimal concentration of $FeCl_3$.

The influence of the reaction temperature on the separation of the three primary components of the biomass was substantial. Heating enhances the dissolution of hemicellulose and lignin by effectively promoting molecular activation.[22] Fig. 3d shows that the separation yield of hemicellulose increases from 48.2% to 81.93% when the temperature rises from 110 °C to 150 °C, representing an increase of 33.73 percentage points. However, the separation efficiency of lignin first increased and then decreased with increasing temperature. This phenomenon can be attributed to the degradation of the porous structure of wood fibers at elevated temperatures, which hinders the dissolution of lignin from the cell wall.[23] The separation rate of cellulose exhibited significant variation with temperature elevation, increasing from an initial value of 5.32% to 12.97%. This result is suboptimal. Consequently, taking into account the separation efficiency of various components, a reaction temperature of 140 °C is deemed optimal.

The influence of the treatment reaction time on the separation efficiency of the DES treatment was investigated (Fig. 3e). The hemicellulose separation rate also exhibited an upward

trend, rising from 53.85% to 88.53%. The separation yield of lignin increased significantly within 60 min; however, it exhibited minimal variation after 60 min. These findings indicated that delignification was effective under the specified conditions. By contrast, the variation in the cellulose separation yield was more pronounced, increasing from 7.35% to 16.72%. In particular, it exhibited a significant increase from 10.38% to 16.72% after 60 min. Thus, the optimal reaction time was determined to be 60 min.

The optimal reaction conditions for CC/TA-$FeCl_3$ are as follows: a molar ratio of CC to TA to $FeCl_3$ of 2 : 1 : 11, a reaction temperature of 140 °C, and a reaction time of 60 min. The separation yields of cellulose, hemicellulose, and lignin were 10.35%, 73.03%, and 71.93%, respectively. The results indicated that CC/TA-$FeCl_3$ exhibited high selectivity for the separation of lignin. Furthermore, the effects of the CC/TA and CC/TA-$FeCl_3$ systems on the eucalyptus separation efficiency were compared. The results are summarized in Table S1.† Compared to the CC/TA treatment, the CC/TA-$FeCl_3$ treatment significantly enhanced the separation efficiency of hemicellulose and lignin within a shorter time frame. The separation yield of hemicellulose increased from 34.25% to 73.03%, whereas that of lignin increased from 13.02% to 71.93%, representing a nearly 60% increase. This was attributed to the addition of $FeCl_3$ to the CC/TA-$FeCl_3$ system, which enhanced the penetration and mass transfer efficiency of the reaction system. These results demonstrate that $FeCl_3$ significantly influences the separation of biomass components. Furthermore, the separation efficiency of the CC/TA-$FeCl_3$ system for lignin was 8.13% greater than that of the CC/LA-$FeCl_3$ system under identical reaction conditions. This was attributed to the presence of additional –OH groups in the structure of tartaric acid, which facilitated more favorable interactions with lignin, thereby enhancing the selectivity of the system toward lignin.[24] Thus, the CC/TA-$FeCl_3$ system demonstrates efficient lignin separation.

Estimating the physicochemical properties of cellulose-rich substrates

The surface morphology of eucalyptus wood before and after treatment was characterized by SEM (Fig. S1†). As can be seen from the picture, the surface of the original eucalyptus is dense and smooth, while tiny holes can be clearly seen on the surface of the treated eucalyptus. The holes on the surface of the treated eucalyptus wood are due to the extraction of hemicellulose and lignin from the eucalyptus wood, which results in the destruction of the cell wall.

The eucalyptus cell wall before and after treatment were observed using CLSM. As can be seen from Fig. S2,† the untreated cell walls are covered with lignin, which also makes the original cell wall structure strong.[25] The fluorescence intensity of lignin gradually weakened, which indicated that lignin was separated from the cell wall after DES treatment. It can also be found from the intensity of fluorescence that the CC/TA-$FeCl_3$ system separates more lignin than the CC/TA method, which also shows that adding $FeCl_3$ to the DES system can effectively promote the separation of lignin.

The structural changes in the substrate before and after treatment were analyzed using FT-IR (Fig. S3†). The signal peaks in the spectra were assigned according to previous studies.[26] 1602 cm^{-1}, 1508 cm^{-1}, 1240 cm^{-1}, and 831 cm^{-1} are respectively attributed to the C–C bond stretching vibration, C–H bond bending vibration, ether bond stretching vibration (usually G lignin unit) in the lignin structure, and C–H deformation caused by lignin aromatic ring vibration and aromatic C–H in-plane deformation (usually S lignin unit). The signal peaks of lignin were significantly weakened after treatment, especially the two peaks belonging to G and S lignin units almost disappeared, which indicated that the separation of lignin was mainly caused by the degradation of G and S lignin.

The crystallinity of cellulose before and after treatment was analyzed by X-ray diffractometer, and the results are shown in Fig. S4.† The CrI value of cellulose is obtained by calculation.[26] Compared with the raw material, the crystallinity index of cellulose in the remaining solid after CC/TA-$FeCl_3$ treatment was significantly improved, indicating that CC/TA-$FeCl_3$ treatment can effectively separate hemicellulose and lignin in the amorphous region. The cell wall structures in the remaining solids after treatment with different methods were characterized by CP/MAS^{13}CNMR (Fig. S5†). The characteristic peaks at 152 ppm, 148 ppm, and 56 ppm are attributed to the syringyl unit (S), guaiacyl unit (G), and methoxy unit in the lignin structure, respectively.[27] The intensity of these peaks gradually weakened after treatment, and was difficult to detect after CC/TA-$FeCl_3$ treatment, indicating that the lignin structure was degraded and separated during CC/TA-$FeCl_3$ treatment.

The effects of CC/TA-$FeCl_3$ treatment on the pyrolysis behavior of biomass were studied, as shown in Fig. S6.† The pyrolysis weight loss after 300 °C is mainly caused by the pyrolysis of cellulose and lignin. It is worth mentioning that the starting temperature of the rapid weight loss interval of the remaining solids was the highest and the end temperature of the rapid weight loss interval was the lowest after CC/TA-$FeCl_3$ treatment, indicating that this treatment method can effectively separate hemicellulose while retaining more cellulose and has a protective effect on cellulose. As shown in Fig. S6b,† the maximum weight loss rate after CC/TA-$FeCl_3$ pretreatment is 12.34% min^{-1} higher than that of the raw material, which indicates that the remaining solid after CC/TA-$FeCl_3$ pretreatment has higher thermal stability.

Fig. S7† shows the contents of carbon and oxygen elements on the surface of eucalyptus wood before and after the reaction. Based on the O/C value of the sample surface, the theoretical lignin coverage on its surface can be calculated.[28] The lignin coverage of the raw material surface was 0.72, and it decreased to 0.50 after CC/TA-$FeCl_3$ treatment, which indicated that the lignin in eucalyptus was separated. In addition, the lignin coverage of the remaining solid surface after CC/LA-$FeCl_3$ pretreatment was higher than that of CC/TA-$FeCl_3$, which was caused by the formation of pseudo-lignin due to weaker intermolecular hydrogen bonds and more active sites in the CC/LA-$FeCl_3$ system.

Analyzing the chemical structure of lignin

Fig. 4a shows the purities of the lignin samples extracted from the DES systems. The figure indicates that the purity of all DES lignin was more than 90%. This shows that the DES treatment could extract high-purity lignin, which is beneficial for the subsequent application of high-quality lignin. The lignin content extracted using CC/TA-$FeCl_3$ is higher than that extracted using CC/TA. This was due to the addition of the catalyst $FeCl_3$ promoting the breaking of lignin-carbohydrate (LCC) bond.

The average relative molecular mass of lignin was determined using GPC to elucidate the depolymerization of lignin in the various DES systems. Fig. 4b shows that the relative molecular weight of lignin extracted using the DES was significantly lower than that of the MWL. This indicates that the lignin macromolecules were cleaved during DES extraction. In particular, the weight- and number-average molecular weights of lignin were significantly reduced by the addition of $FeCl_3$. These results indicate that the addition of $FeCl_3$ enhanced the acidity of the system, thereby facilitating lignin cleavage. The polydispersity coefficients of lignin extracted from CC/TA and CC/LA-$FeCl_3$ were higher than those of milled wood lignin (MWL), indicating poor homogeneity of the lignin and suggesting that its structure may have undergone significant changes.[29] By contrast, the polydispersity coefficient of lignin extracted from the CC/TA-$FeCl_3$ treatment was the lowest (1.73), indicating that the CC/TA-$FeCl_3$ lignin exhibited a narrow molecular weight distribution and high uniformity, as strong hydrogen bonding within the CC/TA-$FeCl_3$ system facilitated the cleavage of lignin into finer and more uniform fragments.

The structure of the lignin extracted from the MWL and DES was analyzed using FT-IR. Characteristic peaks were assigned according to previous studies.[30,31] The results are shown in Fig. 4c. The characteristic peaks at 1604, 1512, and 1454 cm^{-1} correspond to the stretching vibration modes of the lignin aromatic skeleton. The observed peaks suggest that the aromatic structure of lignin (lignin skeleton) was successfully extracted. The basic lignin skeleton was retained during DES treatment. The characteristic peaks at 1325 and 1213 cm^{-1} correspond to the C–H and C–O stretching vibrations associated with the syringyl (S) units. The S units were also observed at 1124 cm^{-1}. The characteristic peak intensity of lignin extracted using CC/TA-$FeCl_3$ was more pronounced than that obtained using CC/LA-$FeCl_3$. This suggests that the lignin extracted through the CC/TA-$FeCl_3$ treatment was enriched in S units.

Thermogravimetric analysis of lignin was performed from 40 °C to 800 °C to investigate the effects of DES on the thermal stability of lignin. The results are shown in Fig. 4d and e. The weight loss observed between 100 °C and 200 °C is attributed

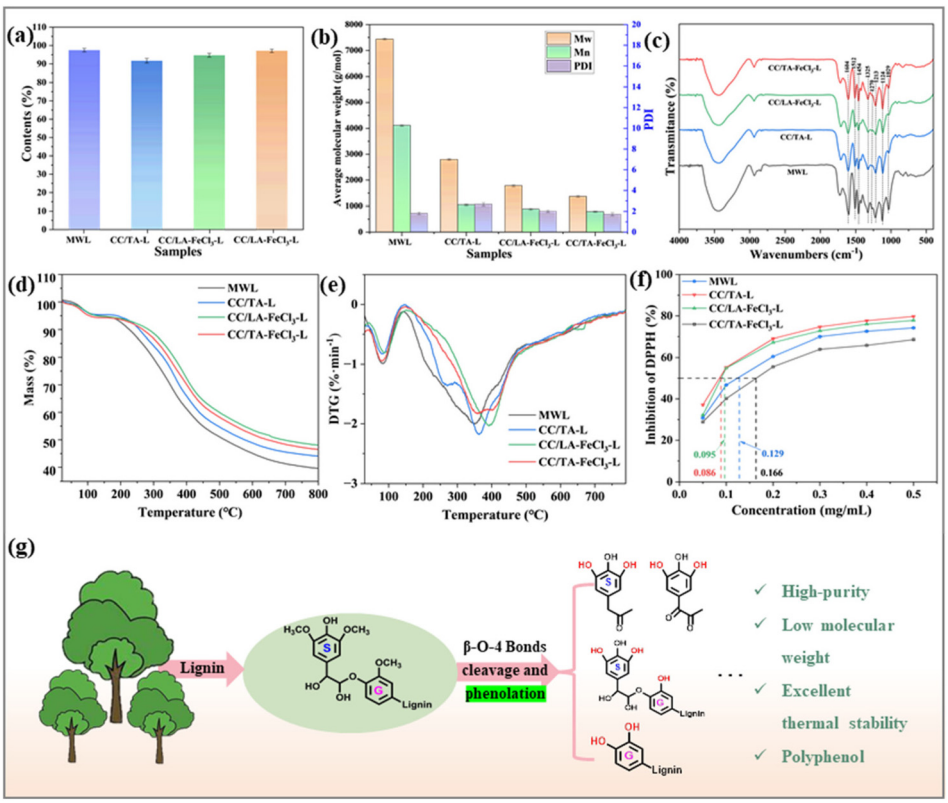

Fig. 4 Chemical structure analysis of lignin extracted from different DES systems. (a) Purity; (b) GPC; (c) FTIR; (d) TGA; (e) DTG; (f) oxidation resistance; (g) schematic of lignin structural changes.

to the presence of low molecular weight impurities in lignin and carbohydrates. However, the weight loss of the lignin samples in this temperature range was not significant, indicating that the extracted lignin was highly pure. The weight loss is pronounced, and the rate of weight loss accelerates significantly between 200 °C and 600 °C. This represents the primary stage of pyrolysis, during which lignin molecules undergo fragmentation.[32] The weight loss peak of the lignin extracted using CC/TA-$FeCl_3$ was observed at a lower temperature than that obtained from CC/TA, which indicates greater removal of side chains in the lignin extracted with DES and $FeCl_3$, while the retained benzene ring structure exhibited enhanced thermal stability. The final solid residue masses of the four lignin samples were 39.69% (MWL), 44.13% (CC/TA-L), 46.65% (CC/TA-$FeCl_3$-L), and 47.99% (CC/LA-$FeCl_3$-L), respectively. Extraction of lignin using CC/TA-$FeCl_3$ resulted in more weight loss than that obtained using CC/LA-$FeCl_3$. This can be attributed to the fact that the lignin extracted using CC/TA-$FeCl_3$ had a lower molecular weight and a reduced degree of polymerization.

The antioxidant properties of the lignin samples extracted using the various methods were assessed using a DPPH radical scavenging assay.[33] Fig. 4f shows that all four lignin samples effectively scavenged the DPPH free radicals. Furthermore, the radical-scavenging capacity increased with increasing lignin concentration. The free radical scavenging capacity of lignin extracted using CC/TA-$FeCl_3$ increased from 37.12% to 79.15% as the initial concentration was raised from 0.05 to 0.5 mg mL^{-1}. The lignin extracted using CC/TA-$FeCl_3$ exhibited the most pronounced antioxidant properties. This suggests that the hydrogen supply capacity of lignin was improved by the incorporation of $FeCl_3$ during DES treatment. Generally, a lower IC_{50} value indicates superior antioxidant performance. Table S2† lists the IC_{50} values of these four lignin as 0.166, 0.129, 0.095, and 0.086 mg mL^{-1}, respectively, which are better than the IC_{50} value of the commercial antioxidant butyl hydroxyanisole (BHA) (0.180 mg mL^{-1}). CC/TA-$FeCl_3$-L exhibited the highest antioxidant activity because it had the lowest IC_{50} value. The antioxidant activity of lignin is significantly influenced by the type and quantity of phenoxy groups present, and enhancing the content of oxygen, hydroxyl, and carboxyl groups in lignin can augment its antioxidant capacity.[34]

Fig. 5a illustrates the aliphatic side chain region (δ_C/δ_H 50–90/2.5–6.0) and the aromatic region (δ_C/δ_H 100–130/5.5–8.0) of DES lignin, with signal peaks assigned according to Table S3.†[35] The lignin extracted using CC/TA retained significant ether and carbon–carbon bonds. The results showed that, in this system, there were fewer breaks in the linkage bonds between the lignin macromolecules. However, upon the addition of $FeCl_3$ to the two DES systems, a significant number of ether and carbon–carbon bonds were eliminated. This is because the addition of $FeCl_3$ provides more active centers and acidic sites to the DES system, facilitating the acid-mediated cleavage of ether linkages within the lignin macromolecules.[36] The signal peak corresponding to the carbon–carbon bond is significantly diminished in CC/TA-$FeCl_3$-L. This indicates that the CC/TA-$FeCl_3$ system has a strong ability to depolymerize lignin owing to its ability to break both ether and carbon–carbon bonds. In the aromatic region, the δ_C/δ_H cross signal peaks of S-units appeared at 104.6/6.51 and 106.4/7.20 ppm. This encompasses both unoxidized and oxidized S-units ($S_{2,6}$ and $S'_{2,6}$). The δ_C/δ_H cross signal peaks of G-units are observed at 111.5/6.99 ppm (C_2–H_2, G_2) and 115.5/6.94 ppm (C_5–H_5, G_5), respectively.[37] The figure clearly illustrates that the signal peaks of the G and S units in the CC/TA-$FeCl_3$-L structure were more pronounced than those in the CC/LA-$FeCl_3$-L structure; the G_2 signal peaks, which were absent in the CC/LA-$FeCl_3$-L structure, were present in the CC/TA-$FeCl_3$-L structure. In summary, the CC/TA-$FeCl_3$ system can extract a more comprehensive lignin structure.

Quantitative phosphorus nuclear magnetic resonance (^{31}P NMR) spectroscopy was used to detect the types and contents of hydroxyl groups in lignin extracted from the milled wood lignin and the different DES treatments (Fig. 5b and c). The attribution of each signal peak was assigned according to Table S4.† The aliphatic hydroxyl content of lignin samples extracted using different methods decreased significantly, which can be attributed to dehydration reactions following the cleavage of the β-O-4 ether bond in lignin.[38] In comparison to MWL, the total phenolic hydroxyl content of lignin samples extracted *via* DES treatment was significantly elevated, which indicates that the β-O-4 bond was cleaved during the lignin extraction process. In comparison to the CC/LA-$FeCl_3$ treatment, the lignin extracted from the CC/TA-$FeCl_3$ treatment exhibited a higher content of phenolic hydroxyl groups, suggesting that its antioxidant performance was superior, which aligns with the results obtained from the DPPH free radical scavenging characterization. Furthermore, the carboxyl group content of the lignin extracted using the CC/TA-$FeCl_3$ method was higher, indicating that a more intense oxidation reaction occurred during extraction using the CC/TA-$FeCl_3$ method. Consequently, the CC/TA-$FeCl_3$ treatment demonstrated greater potential for enhancing the application of polyphenolic hydroxyl lignin.

To elucidate the mechanism underlying the increase in phenolic hydroxyl content of lignin within the CC/TA-$FeCl_3$ system, the cleavage of the β-O-4 bond was investigated using a model compound. The resulting cleavage products were identified through GC-MS analysis, as illustrated in Fig. S8 and S9.† The β-O-4 bond of the model compound was cleaved under the optimal conditions of the CC/TA-$FeCl_3$ system for lignin separation, and the reaction products were extracted using a C18 solid-phase column and analyzed by GC-MS. Specifically, the C18 column was activated with methanol and ultrapure water, and it was washed with 5 mL of ultrapure water after adding a sample. Finally, the sample was eluted with 10 mL of ethyl acetate. This figure demonstrates that the model compound is completely transformed under the reaction conditions, with guaiacol (a) identified as the primary reaction product. After the β-O-4 bond is broken, the oxygen radical at the fourth position of the benzene ring forms a phenolic hydroxyl group in acidic DES, while the carbon on the side chain reacts to form

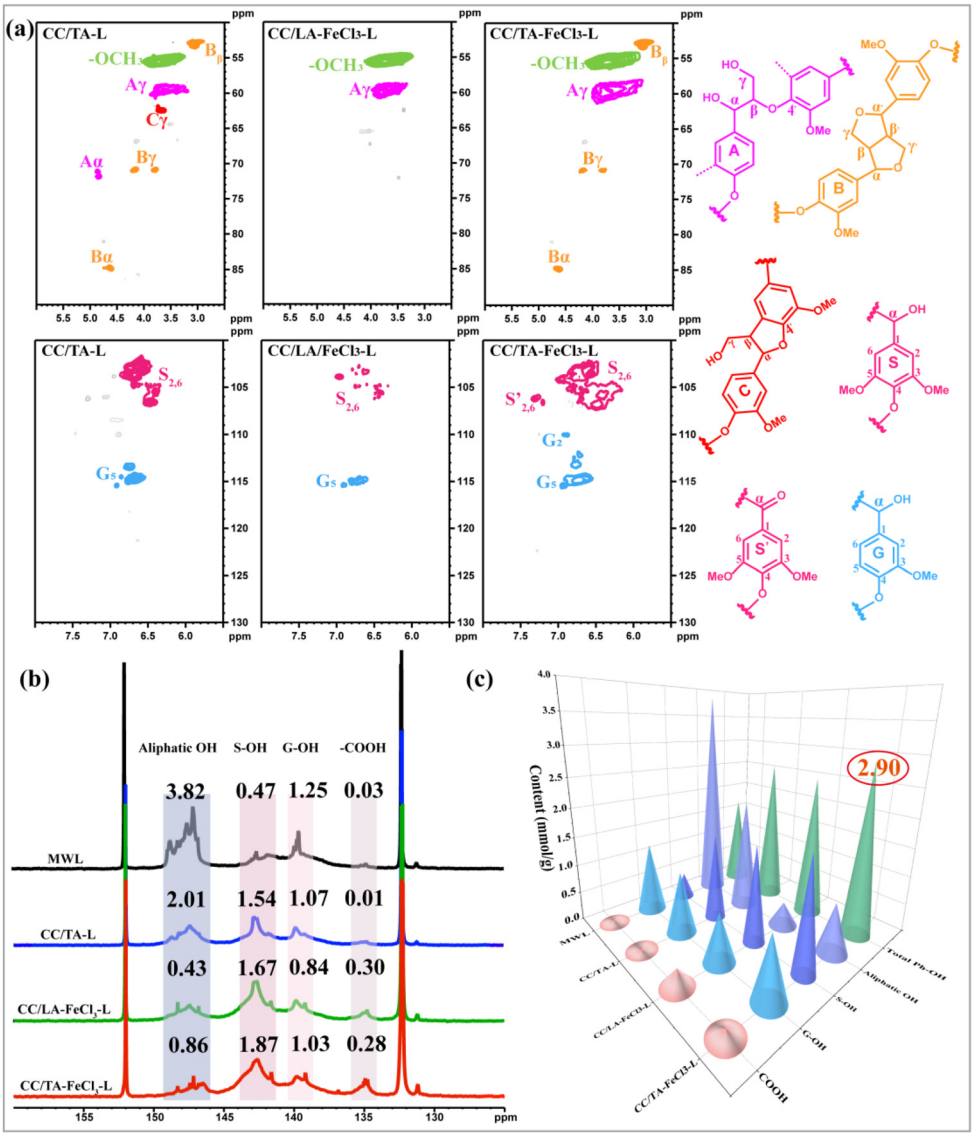

Fig. 5 Nuclear magnetic analysis of lignin extracted from different DES systems; (a) 2D HSQC NMR; (b) ^{31}P NMR spectra; (c) different hydroxyl content *via* ^{31}P NMR.

four products: c, d, e, and f. Previous studies have demonstrated that following the cleavage of the β-O-4 ether bond, the alpha carbon on the side chain can form positively charged carbon electrophiles owing to inductive effects.[39] These carbocation ions undergo further activation to facilitate a range of reactions. Under Lewis acid conditions, transition states form new covalent bonds, and when the acceptor is highly nucleophilic, the beta and gamma carbons depart (forming product c).[40] The nucleophilic addition of the carbonyl group in product c resulted in the formation of product d, with both products coexisting in the CC/TA-$FeCl_3$ system. The formation of products e and f constitutes a redox-neutral process, and diketone products can be obtained in the presence of the reducing metal Fe.[41] These results indicate that the CC/TA-$FeCl_3$ system can yield soluble aromatic products suitable for further upgrading.

Analyzing the performance of LNPs and LNPs/PVA composite films

Fig. 6a and b present SEM and TEM images of the lignin nanoparticles synthesized from different lignin species. As shown in the figure, the LNPs prepared from lignin extracted using different DES systems showed irregular granular or spherical shapes. This is because lignin forms a uniform solution and undergoes molecular association in the solvent. Deionized water is injected into the lignin solution step-by-step, promoting self-assembly and reducing the solubility of lignin.[42] To minimize the contact area with the antisolvent, the hydrophobic regions of lignin (phenylpropane structure) aggregate inward to form micellar nuclei through self-assembly, whereas the hydrophilic functional groups (primarily phenolic and aliphatic hydroxyl groups) extend outward to create micellar

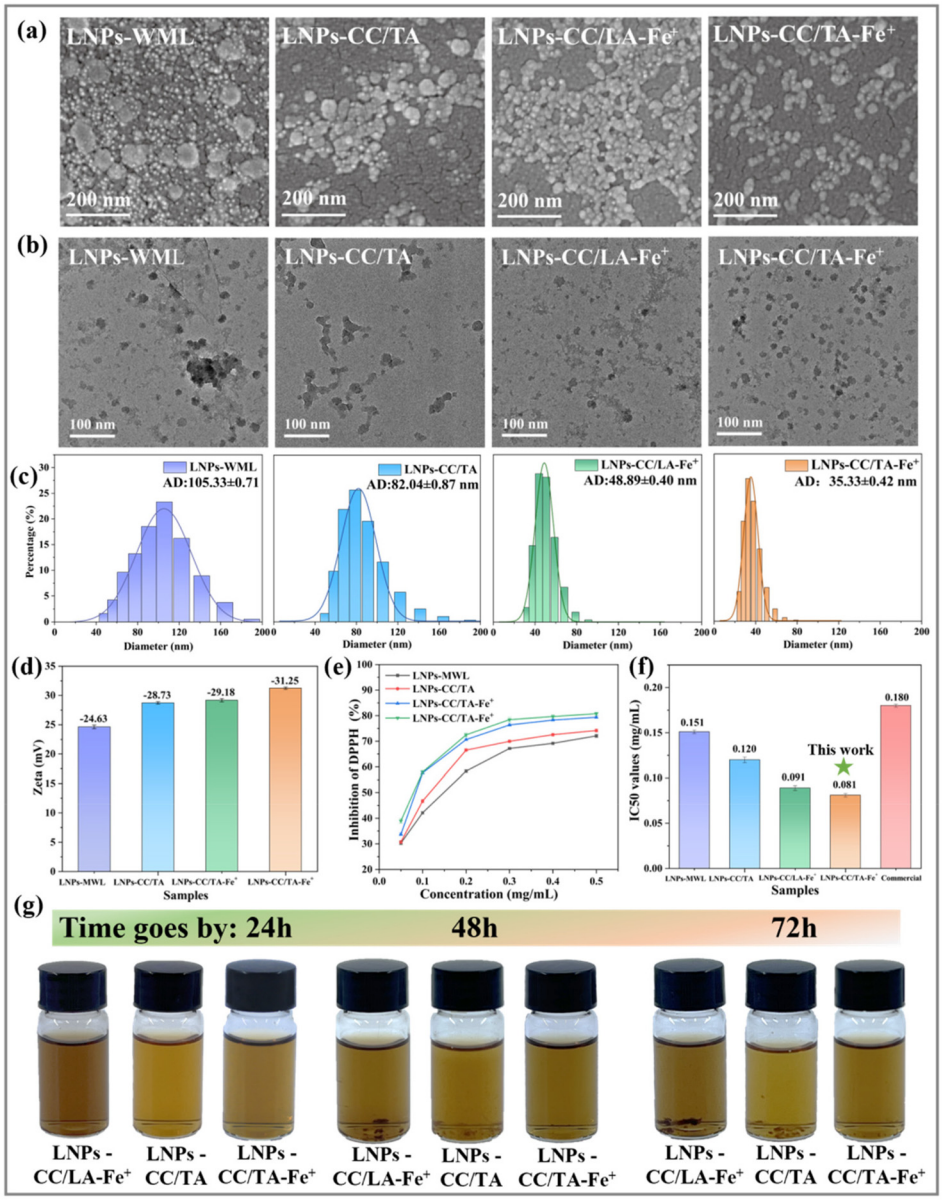

Fig. 6 Chemical characteristics analysis of LNPs. (a) SEM; (b) TEM; (c) grain size distribution map; (d) zeta potential; (e) DPPH free radical scavenging; (f) IC_{50} values; (g) water dispersion stability.

shells. The obtained LNPs had core–shell nanostructures and were spherical.[43] Consequently, the amphiphilic structure of lignin was crucial for the formation of LNPs. The LNPs-MWL nanostructures exhibited partial aggregation; however, some retained the characteristics of primary lignin particles. The morphology of the LNPs-CC/TA was characterized by a flattened shape with an increasing length-to-diameter ratio in the ellipsoidal conformation of the particles. The LNPs-CC/LA-Fe^+ exhibited a relatively loose structure and did not form uniform particles. The LNPs-CC/TA-Fe^+ had a nearly spherical shape and uniform size.

The particle-size distribution of LNPs is illustrated in Fig. 6c. The particle size distribution of the four distinct LNPs ranged from 20 to 200 nm, and the particle size of LNPs is related to the lignin structure. The average particle size of LNPs-MWL was 105.33 nm, while the average particle sizes of LNPs derived from lignin extracted using CC/TA, CC/LA-$FeCl_3$, and CC/TA-$FeCl_3$ decreased by 23.29, 56.44, and 70 nm, respectively, compared to LNPs-MWL. This reduction is attributed to the positive correlation between the particle size of the LNPs and the molecular weight of lignin. Following DES treatment, the molecular weight, chemical structure, and composition of lignin were modified, leading to alterations in the van der Waals interactions and hydrophobic π–π stacking between lignin molecules. These changes result in distinct morphologies and structures of the LNPs.[44] It was observed that

the LNPs prepared with CC/TA-$FeCl_3$ lignin had the narrowest particle size distribution.

In addition, the zeta potential can be used to evaluate the dispersion stability of different LNPs. The greater the absolute value of the zeta potential of the LNPs, the more stable the system is.[45] Fig. 6d shows the zeta potentials of LNPs prepared from various lignin sources. The zeta potential of LNPs prepared from CC/TA-$FeCl_3$ lignin is −31.25 mV, and its absolute value is greater than 30 mV, indicating that lignin molecules prepared by CC/TA-$FeCl_3$ treatment contain more phenolic hydroxyl groups. The surface charge generated by functional groups, such as phenolic hydroxyl groups in the DES lignin molecules, promotes the formation of electric double layers. Consequently, stable lignin nanoparticles were obtained. The long-term stability of LNPs is crucial for expanding their applications in UV shielding, nanofillers, and other domains. The results demonstrate that LNPs with a regular shape, uniform particle size distribution, and high dispersion stability were successfully synthesized by extracting lignin from the CC/TA-$FeCl_3$ system.

The DPPH free radical scavenging capacity and antioxidant properties of the various lignin nanoparticles (LNPs) were assessed, and the results are shown in Fig. 6e and f. As the concentration of LNPs increased from 0.05 to 0.5 mg mL^{-1}, it was observed that the free radical scavenging capacity of LNPs was directly proportional to their hydrogen supply capacity.[46] LNPs-CC/TA-Fe^+ exhibited stronger free radical scavenging capacity, with a DPPH inhibition rate of 79.87% at a concentration of 0.5 mg mL^{-1}. Furthermore, LNPs-CC/TA-Fe^+ exhibited the lowest IC_{50} value, indicating its superior antioxidant performance. Additionally, compared to the antioxidant activity of lignin, the LNPs demonstrated a greater capacity for DPPH free radical scavenging. This enhanced ability may be attributed to the smaller size of the LNPs, their larger relative surface area, and the higher density of exposed phenolic hydroxyl groups per unit area compared with lignin. These results show that the LNPs prepared from DES lignin have good antioxidant properties.

A significant number of oxygen-containing functional groups are distributed on the surface of LNPs, which can establish strong intermolecular hydrogen bonding and physical crosslinking with the hydroxyl groups in the polyvinyl alcohol (PVA) matrix.[47] As illustrated in Fig. 7a, the hydrogen bonding interactions between the neat PVA film and the LNP/PVA film were analyzed using ATR-FTIR. The stretching vibration peak of the hydroxyl (–OH) group in the neat PVA film is observed at 3244 cm^{-1}. The –OH stretching vibration peak gradually shifted to a lower wavenumber region at 3225 cm^{-1} (7% LNPs/PVA), exhibiting a pronounced redshift phenomenon as the content of LNPs increased. This observation indicates the formation of new intermolecular hydrogen bonds between the PVA and LNPs.[48] The C–O bond at 1083 cm^{-1} in the PVA film also exhibited a redshift, shifting from 1083 cm^{-1} in the neat PVA film to 1072 cm^{-1} in the 7% LNPs/PVA film. The observed redshift of the functional groups in the ATR-FTIR spectra corroborated the presence of strong hydrogen bonding interactions between the hydroxyl groups on the PVA macromolecular chain and the oxygen-containing functional groups on the surface of the LNPs.

The transmittance of the LNP/PVA composite film under ultraviolet and visible-light irradiation is shown in Fig. 7b. The neat PVA film was colorless and transparent in the absence of LNPs, exhibiting over 80% transmittance for ultraviolet light within the spectrum of 200–400 nm, and exceeding 90% transmittance for visible light. However, the LNP/PVA film exhibited a significant blocking effect on ultraviolet light, with only 1 wt% LNPs in the composite capable of shielding 60% of the UVC-band ultraviolet radiation. This phenomenon can be attributed to the abundance of phenolic hydroxyl groups within the lignin structure and the conjugated double bonds between the carbonyl group and the benzene ring in the phenylpropane side chain of the LNP structure.[49] The LNP/PVA films effectively shielded nearly all UVB (320–275 nm) and UVC (275–200 nm) bands, while achieving 90% shielding efficiency for UVA (400–320 nm) when the concentration of LNPs was increased to 3 wt%. The LNP/PVA film completely shielded all bands of ultraviolet light when the concentration of LNPs exceeded 5 wt%. While increasing the concentration of LNPs enhanced the ultraviolet light-shielding performance of the composite film, it concurrently compromised its transparency. In the visible region, the transmittance of the LNP/PVA film was lower than that of the neat PVA film, primarily because of the brown color of the LNPs, which imparts a deeper hue to the LNP/PVA film and consequently results in a certain degree of visible-light absorption.[50] The LNP/PVA film demonstrated exceptional UV-shielding performance.

In order to study the ability of PVA film to resist the strength of water molecules, Fig. 7c shows the water contact angle of pure PVA film and LNPs/PVA film at t = 0 s. PVA film has a high hydrophilicity due to its rich hydroxyl group, which can form hydrogen bonds in water, and the contact angle is 50.5° when the water droplets contact the pure PVA film. After LNPs was added to PVA film, the contact angle of LNPs/PVA film gradually increased with the increase of LNPs addition. This is due to the hydrogen bonding between PVA and hydrophobic lignin in the composite film, and the number of accessible sites that can form hydrogen bonds with water is reduced. At the same time, the composite film becomes coarser with the increase of lignin nanofillers, resulting in increased contact angle.

Fig. 7d and e show the thermal stabilities of the LNP/PVA films. Partial side-chain breakage and hydroxyl elimination of PVA and LNPs occur at 170 °C–360 °C.[51] The temperature corresponding to the maximum weight loss of the composite film was observed to be within this range. The TGA results indicate that the thermal stability of the PVA film is significantly enhanced by the addition of LNPs. The initial degradation temperature of the PVA film was measured at 261.38 °C. With the addition of LNPs, the initial degradation temperature increased significantly, continuing to rise as the amount of LNPs increased. The maximum degradation temperature

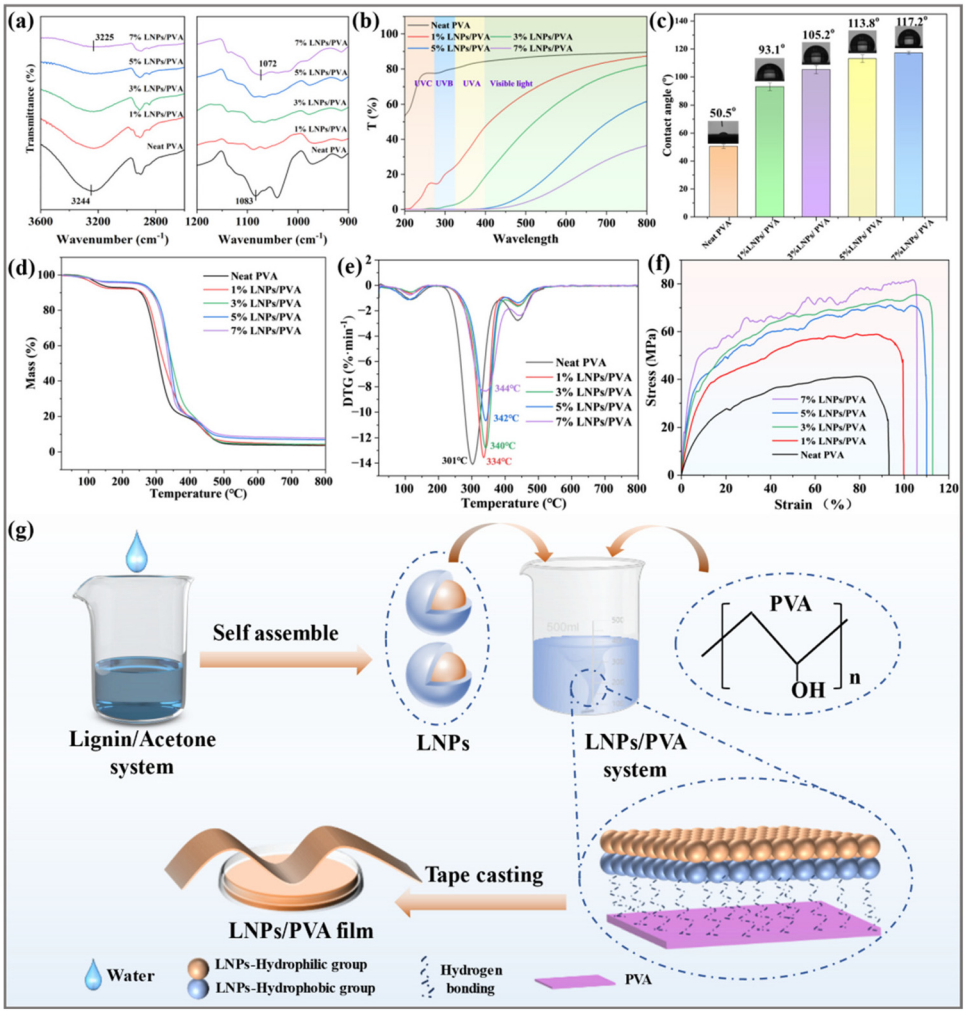

Fig. 7 Structure and performance analysis of LNPs/PVA composite film. (a) FT-IR spectra; (b) light transmittance; (c) water contact angle; (d) TGA; (e) DTG; (f) stress–strain curve; (g) schematic of LNPs/PVA composite film formation.

exhibited a similar trend. The T_{max} of the neat PVA film is 301.8 °C, while that of the LNP/PVA film is 343.75 °C when the LNPs content is 7 wt%. This enhancement can be attributed to the formation of robust hydrogen bonds between the LNPs and PVA, along with the presence of phenylpropane structural units within the LNPs, which collectively contribute to the improved thermal stability of the composite film.[52]

The stress–strain curves and mechanical property parameters of the LNP/PVA composite films are shown in Fig. 7f and 8. The tensile strength and elongation at break of the neat PVA films were 41.14 MPa and 93.10%, respectively. The tensile strength and elongation at break of the LNP/PVA film were significantly enhanced, demonstrating superior mechanical properties compared to those of the neat PVA film. The tensile strength of the LNP/PVA composite film increased with the addition of LNPs, and its tensile strength was 75.38 MPa when the addition of LNPs was 3 wt%. Notably, the tensile strength of the 7 wt% LNP/PVA film reached 81.74 MPa, which was double that of the neat PVA film, demonstrating enhanced stress–strain capacity. The crimping, bending, stretching, and folding properties are illustrated in Fig. 8a–d. Surprisingly, the composite film could be stretched to twice its length, and no permanent deformation occurred after the stretching (Fig. 8e). Fig. 8f and g show the load-bearing capacities of the LNP/PVA composite film. A composite film strip measuring 10 × 2 cm (length × width) could support a weight of 2.5 kg without breaking. Furthermore, the LNP/PVA composite film did not collapse or deform under a surface load of 200 g. Therefore, the LNP/PVA composite film had excellent mechanical properties owing to the good synergy between the rigid polyphenolic LNPs and the ductile PVA.[53]

The LNPs/PVA composite film was applied in different scenarios to evaluate its application performance, and the results are shown in Fig. S10.† The air tightness and porosity of the composite film were reduced due to the addition of LNPs, which increased the thermal insulation and water retention properties of the LNPs/PVA film, which was beneficial to promote the germination and growth of crops. Fig. S10a†

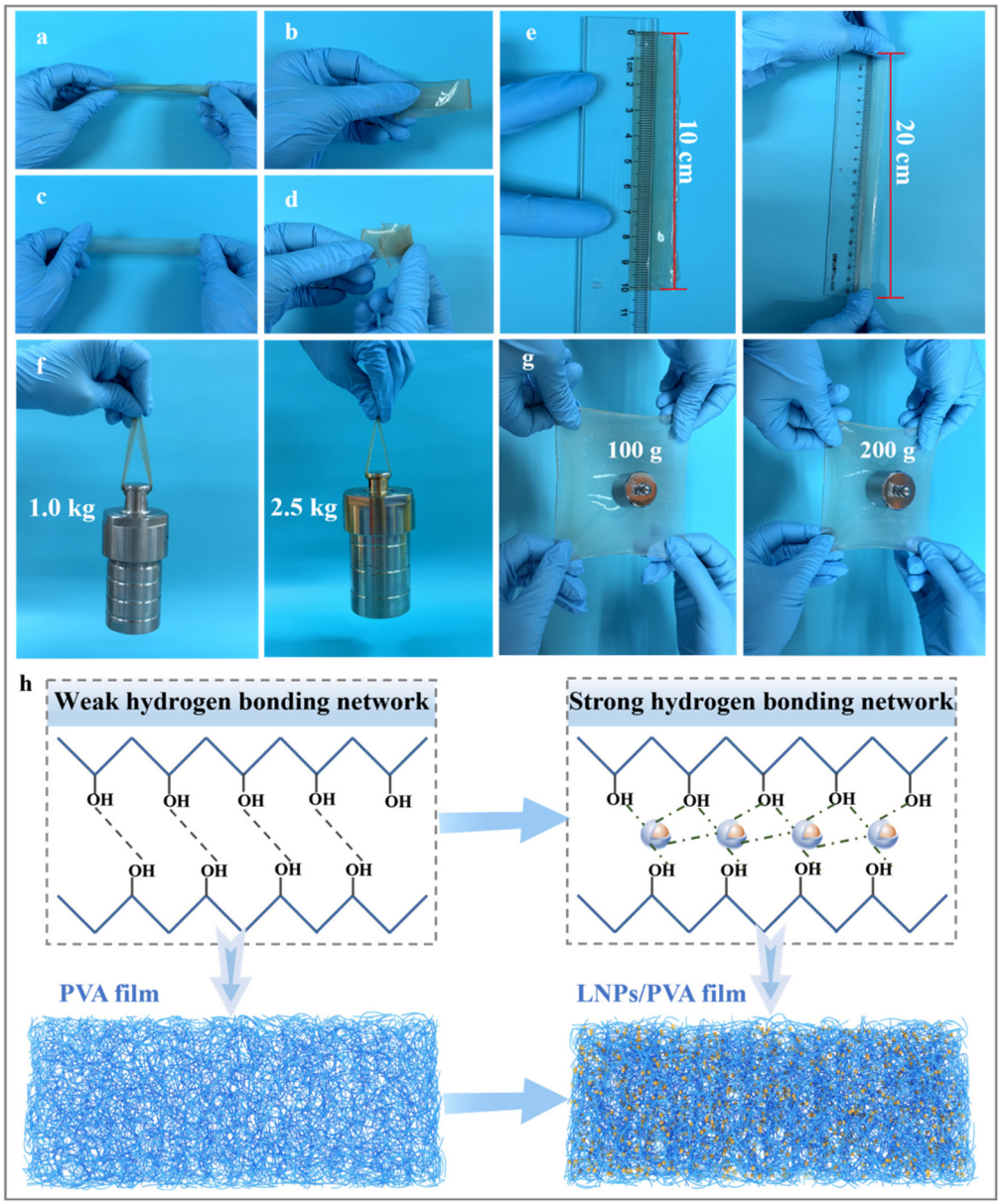

Fig. 8 Demonstration of the superior mechanical properties of LNP/PVA composite films. (a) Curling; (b) bending; (c) stretching; (d) folding; (e) elongation to twice the original length; (f) withstanding tension; (g) withstanding pressure; (h) interweaving diagram of LNPs and PVA.

Evaluation of the germination rate of Brassica rapa using commercially available PVA mulch, polyethylene mulch, and our prepared LNPs/PVA composite film. The growth of Brassica rapa was recorded on days 0, 3, 6, and 9. The results showed that the germination rate of cabbage was higher in the area covered by the LNPs/PVA composite film. This indicates that the LNPs/PVA film was prepared in this work has good thermal insulation and water retention properties and can promote crop growth. Furthermore, the biodegradability is a key indicator for evaluating the application ability of LNPs/PVA film. Different types of films were buried in soil and placed in natural environments with the goal of documenting their biodegradation properties. The biodegradation performance of different types of films was recorded at 0, 30, 60, and 90 days, and the results are shown in Fig. S10b.† The LNPs/PVA film was almost completely degraded on the 90th day, while the commercially available PVA film was only degraded about 70% at this time, indicating that the LNPs/PVA film prepared in this work has excellent biodegradability. Fig. S10c† shows the antioxidant properties of the LNPs/PVA film. Bananas protected by LNPs/PVA film were oxidized more slowly than those exposed to air and protected by commercial plastic wrap, which indicating that lignin still has antioxidant properties when it is prepared as LNPs and composited to PVA films. In summary, the LNPs/PVA composite film with wide application potential in green agriculture was prepared.

Materials and methods

Materials

The eucalyptus was sourced from a forest farm in Nanning, Guangxi. Eucalyptus flour with particle sizes ranging from 40 to 60 mesh was obtained by mechanical grinding and was stored in sealed bags for future use. The chemical composition of the raw material was analyzed using the methodology established by the National Renewable Energy Laboratory (NREL), and the results indicated that cellulose constituted 46.37%, hemicellulose accounted for 11.85%, and lignin comprised 35.04%. TA, lactic acid (LA), CC, and ferric chloride hexahydrate ($FeCl_3 \cdot 6H_2O$) were obtained from Sigma-Aldrich, while other reagents were sourced from Aladdin.

Preparation and characterization of CC/TA-$FeCl_3$ DES

CC, TA or LA, and $FeCl_3$ were added to reaction vessels in specific molar ratios. The mixture was stirred in an oil bath at 90 °C for 1 to 2 h until a clear and transparent liquid was obtained. The resulting liquid was stored in a dry environment until further use after cooling. Subsequently, the chemical properties of the various DES systems were analyzed using Fourier-transform infrared spectroscopy based on ATR method (TENSOR II, Bruker, Berlin, Germany) over a scanning wavelength range of 400 to 4000 cm^{-1}. The viscosity of the DES was analyzed using a rapid viscosity analyzer (RVA-TecMaster, Perten, Melbourne, Australia) with temperature protocols and stirring rates applied following standard methods. The densities of the different DES were determined using a gravimetric method, while their conductivities were measured using a conductivity meter (DDB-305A, Leici, Shanghai, China).

The molecular properties of the DES were assessed by analyzing the Kamlet–Taft (K–T) parameters as outlined by Fernandes *et al.*[54] Nile red, *N*,*N*-dimethyl-4-nitroaniline, and 4-nitroaniline were individually dissolved in ethanol at a concentration of 1 mg mL^{-1}. Subsequently, a 5 μL dye solution was added to 1000 μL of DES and subjected to ultrasound treatment for 30 min at room temperature to ensure thorough mixing. Finally, an ultraviolet spectrophotometer (Cary 5000, Agilent, California, USA) was used to analyze the maximum absorption wavelengths of the dye and DES solutions. The absorption spectrum of the Nile red dye sample was recorded in the range of 400–650 nm. The absorption wavelengths of the *N*,*N*-dimethyl-4-nitroaniline and 4-nitroaniline samples were recorded in the range of 300–450 nm.

Fractionation of eucalyptus lignin using CC/TA-$FeCl_3$ DES

CC/TA-$FeCl_3$ DES reaction for the separation of eucalyptus was conducted in a 100 mL polytetrafluoroethylene reactor. Two grams of eucalyptus wood flour and 20 g of DES were combined in the reactor, which was subsequently placed in a high-temperature oven and heated to the desired reaction temperature. Upon completion of the reaction, the reactor was removed and cooled to room temperature using tap water, after which the mixture was diluted with 50 mL of ethanol. The mixture was filtered, after which the cake was washed three times with a mixture of ethanol and water (7 : 3), using 50 mL of the mixture for each wash. The residual carbohydrate solids were then recovered and dried in a 35 °C oven, after which the dried solids were stored in sealed bags for subsequent analysis of hemicellulose and lignin separation yields. The ethanol in the filtrate was evaporated using a rotary evaporator to obtain a DES-lignin mixture. Subsequently, the lignin in the mixture was extracted by adding nine times its volume of distilled water, and the precipitated solids were separated by centrifugation. The solids obtained by freeze-drying after centrifugation were designated as DES-regenerated lignin.

Structural analysis of DES regenerated lignin

The purity, thermal stability, and polydispersity of the DES-regenerated lignin were analyzed using UV–VIS spectroscopy (Agilent 8453, Agilent, California, USA), thermogravimetric analysis (DTG-60H, Shimadzu, Kyoto, Japan), and gel permeation chromatography (Agilent 1260, Agilent, California, USA). The lignin in the substrate was extracted using the milled wood lignin (MWL) method, and the structures of MWL and DES lignin were characterized by 2D HSQC NMR and ^{31}P NMR (AVANCE III HD500, Bruker, Salbruken, Germany), to understand the structural transformations of lignin during different treatment processes. Unstable hydrogen atoms (such as –OH, –COOH, –SH and other groups) in lignin samples can react with phosphating agents to generate lignin phosphorus-containing derivatives. Therefore, the phenolic hydroxyl, carboxyl and other functional groups in the lignin samples can be detected using ^{31}P NMR spectroscopy technology. The antioxidant properties of the lignin samples were evaluated using the 2,2-diphenyl-1-picrylhydrazyl (DPPH) radical scavenging method.[55] Additionally, the products resulting from the cleavage of β-O-4 lignin model bonds were analyzed using gas chromatography-mass spectrometry (GC-MS). The temperature program was as follows: injection port temperature 250 °C, initial oven temperature 50 °C (maintained for 1 min), then raised to 300 °C at a rate of 15 °C min^{-1} (maintained for 7 min), detection temperature 290 °C.

Preparation of lignin nanoparticles

Lignin was dissolved in 80% acetone (1 mg mL^{-1}) and dispersed by ultrasonication, followed by the addition of 40 mL of deionized water *via* a peristaltic pump. After the addition of deionized water, the pH of the lignin solution was adjusted to 6 using a 4% NaOH solution, and the mixture was stirred for 30 min. The lignin nanoparticles were obtained at room temperature *via* acetone evaporation. LNPs prepared from milled wood lignin (MWL) were designated as LNPs-MWL; LNPs derived from CC/TA-$FeCl_3$ lignin were referred to as LNPs-CC/TA-Fe^+; LNPs obtained from CC/TA lignin were labeled as LNPs-CC/TA; and LNPs synthesized from CC/LA-$FeCl_3$ lignin were named LNPs-CC/LA-Fe^+.

Preparation of LNPs/PVA composite film

LNPs/PVA composite films were prepared using a simple casting method.[56] A 3% polyvinyl alcohol (PVA) aqueous solu-

tion was prepared and stirred in a water bath at 90 °C for 2 h. After the PVA had completely dissolved, colloidal LNP dispersions with varying mass fractions were subsequently added. The PVA solution was mixed with the LNP colloidal dispersion and stirred for 1 h in a water bath maintained at 90 °C. At the end of the reaction, the mixture was cooled to room temperature. The PVA mixture was then subjected to ultrasonic treatment for 30 min to eliminate excess air bubbles. The PVA mixture was cast into a polytetrafluoroethylene (PTFE) mold measuring 10 cm × 10 cm. The LNPs/PVA composite film was obtained and subsequently dried in a vacuum oven at 55 °C for 12 h. After drying, the composite film was conditioned for 12 h to reach moisture equilibrium before characterization. The composite films were labeled according to the mass ratio of the LNPs to PVA; for example, 1% LNP/PVA indicates a PVA composite film with 1 wt% LNPs. A pure PVA film (Neat PVA) was used as a control.

Performance analysis of LNPs and LNPs/PVA composite films

The morphology of LNPs was analyzed using scanning electron microscopy (SEM) and transmission electron microscopy (TEM). The particle size and zeta (ζ) potential of LNPs were assessed using a nanoparticle analyzer (Zetasizer Lab, Nano ZS90, England), with deionized water serving as the dispersant. Furthermore, LNPs were incorporated into PVA films to evaluate their potential for enhancing the performance of PVA films. The morphology, functional group characteristics, and thermal stability of the LNP/PVA films were analyzed using SEM, Fourier-transform infrared (FT-IR) spectroscopy, and thermogravimetric analysis (TGA). Finally, the UV resistance, mechanical properties, and hydrophobic characteristics of the LNP/PVA films were characterized using attenuated total reflection Fourier-transform infrared spectroscopy (ATR-FTIR), ultraviolet–visible spectrophotometry, a universal testing machine, and a contact angle goniometer.

Conclusions

A novel and efficient DES that green extraction lignin with higher purity (up to 97%) than the comparison system, while retaining a more complete fiber structure. The $FeCl_3$-mediated TA-DES has a stronger hydrogen bond network, which is conducive to the cleavage of β-O-4 bond. The extracted lignin has a lower molecular weight and higher phenolic hydroxyl content, which promotes the green value-added transformation of lignin. In addition, the LNPs prepared using CC/TA-$FeCl_3$-L exhibited uniform morphology and good dispersion stability. Finally, incorporating LNPs into PVA films improved the UV barrier properties, thermal stability, hydrophobicity, and biocompatibility of the PVA films, providing more possibilities for their application. Consequently, the CC/TA-$FeCl_3$ holds significant promise in the realm of biomass refining and facilitates the high-quality application of lignin.

Author contributions

Yadan Luo: conceptualization and writing – review & editing; Baojie Liu and Linlin Liang: investigation and writing – original draft; Chengrong Qin: funding acquisition and resources; Huaying Luo and Fanyan Zeng: validation; Caoxing Huang and Chen Liang: formal analysis; Shuangquan Yao: project administration and supervision.

Data availability

All relevant data are within the manuscript and its Additional files.

Conflicts of interest

There are no conflicts to declare.

Acknowledgements

This project was sponsored by the National Key Research and Development Program (2022YFC2105505). This project was supported by the Guangxi Natural Science Foundation of China (2023GXNSFGA026001).

References

1 Y. Liao, S.-F. Koelewijn, G. Van den Bossche, J. Van Aelst, S. Van den Bosch, T. Renders, K. Navare, T. Nicolai, K. Van Aelst, M. Maesen, H. Matsushima, J. M. Thevelein, K. Van Acker, B. Lagrain, D. Verboekend and B. F. Sels, *Science*, 2020, **367**, 1385–1390.
2 N. Li, K. Yan, T. Rukkijakan, J. Liang, Y. Liu, Z. Wang, H. Nie, S. Muangmeesri, G. Castiella-Ona, X. Pan, Q. Zhou, G. Jiang, G. Zhou, J. Ralph, J. S. M. Samec and F. Wang, *Nature*, 2024, **630**, 381–386.
3 N. Obrzut, P. F. F. Carnelli, S. Brauer, J. M. Notestein, G. F. Wells and K. A. Gray, *ACS Sustainable Chem. Eng.*, 2023, **11**, 491–501.
4 Y. Li, S. Zhao, D. Hu, A. J. Ragauskas, D. Cao, W. Liu, C. Si, T. Xu, P. Zhao, X. Song and K. Li, *ACS Sustainable Chem. Eng.*, 2022, 11856–11866.
5 X. Yu, S. Chen, W. Wang, T. Deng and H. Wang, *J. Cleaner Prod.*, 2022, **339**, 130769.
6 Z. Li, E. Sutandar, T. Goihl, X. Zhang and X. Pan, *Green Chem.*, 2020, **22**, 7989–8001.
7 G. Meng, W. Lan, L. Zhang, S. Wang, T. Zhang, S. Zhang, M. Xu, Y. Wang, J. Zhang, F. Yue, Y. Wu and D. Wang, *J. Am. Chem. Soc.*, 2023, **145**, 12884–12893.
8 R. Wang, H. Qin, Z. Song, H. Cheng, L. Chen and Z. Qi, *Chem. Eng. J.*, 2022, **445**, 136664.
9 X.-J. Shen, J.-L. Wen, Q.-Q. Mei, X. Chen, D. Sun, T.-Q. Yuan and R.-C. Sun, *Green Chem.*, 2019, **21**, 275–283.

10 Y. Feng, T. L. Eberhardt, F. Meng, C. Xu and H. Pan, *Bioresour. Technol.*, 2024, **400**, 130666.
11 C. He, F. Shen, D. Tian, M. Huang, L. Zhao, Q. Yu and F. Shen, *Int. J. Biol. Macromol.*, 2024, **254**, 127853.
12 F. Shen, S. Wu, M. Huang, L. Zhao, J. He, Y. Zhang, S. Deng, J. Hu, D. Tian and F. Shen, *Green Chem.*, 2022, **24**, 5242–5254.
13 E. R. Alonso, I. Leon, L. Kolesnikova, S. Mata and J. L. Alonso, *Angew. Chem., Int. Ed.*, 2021, **60**, 17410–17414.
14 B. Myrzakhmetov, M. Karibayev, Y. Wang and A. Mentbayeva, *Eurasian Chem.-Technol. J.*, 2024, **26**, 29–36.
15 M. Yao, B. Liu, L. Qin, Z. Du, Z. Wang, C. Qin, C. Liang, C. Huang and S. Yao, *Green Chem.*, 2024, **26**, 4528–4543.
16 D. Yu, D. Jiang, Z. Xue and T. Mu, *Green Chem.*, 2024, **26**, 7478–7507.
17 C. Zhu, X. He, Y. Shi, Z. Wang, B. Hao, W. Chen, H. Yang, L. Zhang, H. Ji, J. Liu, C. Yan, J. Zhou and T. Qian, *ACS Nano*, 2023, **17**, 21614–21625.
18 D. J. G. P. van Osch, C. H. J. T. Dietz, J. van Spronsen, M. C. Kroon, F. Gallucci, M. v. S. Annaland and R. Tuinier, *ACS Sustainable Chem. Eng.*, 2019, **7**, 2933–2942.
19 Y. Dai, J. van Spronsen, G.-J. Witkamp, R. Verpoorte and Y. H. Choi, *Anal. Chim. Acta*, 2013, **766**, 61–68.
20 X. Chen, J. Jiang, J. Zhu, W. Song, C. Liu and L.-P. Xiao, *Bioresour. Technol.*, 2022, **362**, 127788.
21 J. Zheng, L. Chen, X. Qiu, Y. Liu and Y. Qin, *Bioresour. Technol.*, 2023, **385**, 129458.
22 J. Lee and K. Y. Park, *Chemosphere*, 2020, **256**, 127116.
23 Y. Luo, B. Liu, B. Deng, X. Long, Z. Du, C. Qin, C. Liang, C. Huang and S. Yao, *Ind. Crops Prod.*, 2024, **208**, 117791.
24 Z. Ling, W. Tang, Y. Su, L. Shao, P. Wang, Y. Ren, C. Huang, C. Lai and Q. Yong, *Bioresour. Technol.*, 2021, **333**, 125122.
25 Z. Zhang, J. Xu, J. Xie, S. Zhu, B. Wang, J. Li and K. Chen, *Carbohydr. Polym.*, 2022, **290**, 119472.
26 J. Cheng, C. Huang, Y. Zhan, S. Han, J. Wang, X. Meng, C. G. Yoo, G. Fang and A. J. Ragauskas, *Chem. Eng. J.*, 2022, **443**, 136395.
27 B. Liu, J. Li, L. Liu, M. Yao, J. Liang, C. Qin, C. Liang, C. Huang, Z. Zhang and S. Yao, *Ind. Crops Prod.*, 2022, **187**, 115406.
28 Q. Chu, W. Tong, S. Wu, Y. Jin, J. Hu and K. Song, *Green Chem.*, 2021, **23**, 4074–4086.
29 D. Huang, R. Li, P. Xu, T. Li, R. Deng, S. Chen and Q. Zhang, *Chem. Eng. J.*, 2020, **402**, 126237.
30 M. Thierry, A. Majira, B. Pegot, L. Cezard, F. Bourdreux, G. Clement, F. Perreau, S. Boutet-Mercey, P. Diter, G. Vo-Thanh, C. Lapierre, P.-H. Ducrot, E. Magnier, S. Baumberger and B. Cottyn, *ChemSusChem*, 2018, **11**, 439–448.
31 H. Li, X. Li, T. You, D. Li, H. Nawaz, X. Zhang and F. Xu, *Int. J. Biol. Macromol.*, 2021, **193**, 319–327.
32 X. Chen, Q. Liu, B. Li, N. Wang, C. Liu, J. Shi and L. Liu, *Int. J. Biol. Macromol.*, 2024, **259**, 129354.
33 Y. Liu, N. Deak, Z. Wang, H. Yu, L. Hameleers, E. Jurak, P. J. Deuss and K. Barta, *Nat. Commun.*, 2021, **12**, 5424.
34 W. Jiang, M. V. Misovich, A. P. S. Hettiyadura, A. Laskin, A. S. McFall, C. Anastasio and Q. Zhang, *Environ. Sci. Technol.*, 2021, **55**, 5199–5211.
35 X. Du, S. Wu, T. Li, Y. Yin and J. Zhou, *Fuel Process. Technol.*, 2022, **231**, 107232.
36 L. Shuai, M. T. Amiri, Y. M. Questell-Santiago, F. Heroguel, Y. Li, H. Kim, R. Meilan, C. Chapple, J. Ralph and J. S. Luterbacher, *Science*, 2016, **354**, 329–333.
37 Z. Chen, X. Bai, A. Lusi, H. Zhang and C. Wan, *ACS Sustainable Chem. Eng.*, 2020, **8**, 9783–9793.
38 A. Rahimi, A. Ulbrich, J. J. Coon and S. S. Stahl, *Nature*, 2014, **515**, 249–252.
39 D. Tian, J. Hu, J. Bao, R. P. Chandra, J. N. Saddler and C. Lu, *Biotechnol. Biofuels*, 2017, **10**, 192.
40 M. Ma, L. Dai, J. Xu, Z. Liu and Y. Ni, *Green Chem.*, 2020, **22**, 2011–2017.
41 X. Liu, M. Xie, Y. Hu, S. Li, S. Nie, A. Zhang, H. Wu, C. Li, Z. Xiao and C. Hu, *Ind. Crops Prod.*, 2022, **183**, 114943.
42 Y. Ma, Y. Liao, Z. Jiang, Q. Sun, X. Guo, W. Zhang, C. Hu, R. Luque, B. Shi and B. F. F. Sels, *Green Chem.*, 2023, **25**, 993–1003.
43 W. Yang, E. Fortunati, F. Bertoglio, J. S. Owczarek, G. Bruni, M. Kozanecki, J. M. Kenny, L. Torre, L. Visai and D. Puglia, *Carbohydr. Polym.*, 2018, **181**, 275–284.
44 Y. Guo, Y. You, G. Guo, Z. Chen, W. Peng, L. Hu, S. Liang and H. Xie, *Int. J. Biol. Macromol.*, 2023, **237**, 124218.
45 X. Zhang, W. Liu, D. Yang and X. Qiu, *Adv. Funct. Mater.*, 2019, **29**, 1806912.
46 W. Zhang, P. Gao, Q. Jiang and W. Xia, *Food Hydrocolloids*, 2023, **139**, 108548.
47 Y.-H. Xu, M.-F. Li and F. Peng, *Chem. Eng. J.*, 2023, **473**, 145233.
48 J. Yan, T. Bai, J. Lu, D. Wang, S. Huan, H. Yu, W. Cheng, Y. Yue and G. Han, *Chem. Eng. J.*, 2024, **494**, 152993.
49 J. Huang, Q. Guo, R. Zhu, Y. Liu, F. Xu and X. Zhang, *Int. J. Biol. Macromol.*, 2021, **189**, 635–640.
50 L. A. Worku, M. G. Tadesse, A. Bachheti, D. P. Pandey, A. K. Chandel, A. W. Ewuntu and R. K. Bachheti, *Int. J. Biol. Macromol.*, 2024, **254**, 127644.
51 Y. Zhou, Y. Han, J. Xu, W. Han, F. Gu, K. Sun, X. Huang and Z. Cai, *Int. J. Biol. Macromol.*, 2023, **232**, 123105.
52 X. Zhang, M. Yang, Q. Yuan and G. Cheng, *ACS Sustainable Chem. Eng.*, 2019, **7**, 17166–17174.
53 P. Jiang, P. Lin, C. Yang, H. Qin, X. Wang and F. Zhou, *Chem. Mater.*, 2020, **32**, 9983–9995.
54 C. C. Fernandes, A. Paiva, R. Haghbakhsh and A. R. C. Duarte, *J. Mol. Liq.*, 2023, **384**, 122280.
55 Y.-H. Xu, P. Zeng, M.-F. Li, J. Bian and F. Peng, *Sep. Purif. Technol.*, 2021, **279**, 119780.
56 H. Cheng, Y. Zhao, X. Wei, Q. Zhang, E. Yang, Y. Xiong, J. Zhu, Z. Wu, J. Chen and W. Chen, *Macromolecules*, 2024, **57**, 1569–1580.